

Ankylography: three-dimensional structure determination from a single view

Kevin S. Raines¹, Sara Salha¹, Huaidong Jiang¹, Richard L. Sandberg², Henry C.

Kapteyn², Margaret M. Murnane², Jincheng Du³ and Jianwei Miao¹

¹*Department of Physics and Astronomy and California NanoSystems Institute, University of California, Los Angeles, CA 90095, USA.* ²*Department of Physics and JILA, University of Colorado and NIST, Boulder, CO 80309, USA.* ³*Department of Materials Science & Engineering, University of North Texas, Denton, TX 76203, USA*

The ability to determine the structure of matter in three dimensions has profoundly advanced our understanding of nature. Traditionally, the foremost schemes used for 3D structure determination of general specimens are implemented either by acquiring multiple measurements over various sample orientations, as in the case of crystallography and tomography^{1,2}, or by scanning a series of thin sections through the sample, as in confocal microscopy³. Here we present a novel 3D imaging modality, denoted ankylography^{*}, which enables complete 3D structure determination from a single sample orientation using a monochromatic incident beam. We show that when the diffraction pattern of a finite object is sampled at a sufficiently fine scale on the Ewald sphere, the 3D structure of the object is determined by the 2D spherical pattern. We confirm the theoretical analysis by performing a 3D numerical reconstruction of a sodium silicate glass structure at 2 Å resolution from a 2D spherical diffraction pattern

^{*} Ankylography is derived from the Greek words *ankylos* which means “curved” and *graphein* which means “writing”.

alone. Using a soft X-ray laser, we experimentally demonstrate ankylography by obtaining a 3D image of a test sample from only a single 2D diffraction pattern. This approach of obtaining complete 3D structure information from a single view is anticipated to find broad applications in the physical and life sciences. As X-ray free electron lasers (X-FEL) are under rapid development worldwide, ankylography opens a door to determining the 3D structure of a biological specimen from a single pulse and allowing for time-resolved 3D structure determination of disordered materials.

Lensless imaging techniques generally begin with the coherent diffraction pattern of a non-crystalline sample, which is measured and then directly phased to obtain an image. The initial insight that the continuous diffraction pattern of a non-crystalline object might be invertible was suggested by Sayre in 1980 (ref. 4). In 1999, coherent diffraction microscopy was experimentally demonstrated by Miao *et al.*⁵. Since that initial demonstration, lensless imaging has advanced considerably, and has been applied to a wide range of samples including nanoparticles, nanocrystals, biomaterials, cells, cellular organelles, viruses and carbon nanotubes by synchrotron radiation⁶⁻¹⁹, electrons^{20,21}, optical lasers^{21,22}, high harmonic and short wavelength laser sources^{23,24}, and free electron lasers²⁵⁻²⁷. However, in order to generate 3D images by coherent diffraction microscopy, multiple diffraction patterns are required at different sample orientations^{7,10-13,16,19}. The precise mechanical tilting necessary to obtain these patterns prevents 3D imaging by a single X-FEL pulse or time-resolved 3D structure determination of disordered materials. Here we develop a novel imaging modality, ankylography, in order to overcome these limitations.

Figure 1 shows a schematic layout of the experimental set-up for ankylography. A coherent beam of wavelength λ illuminates a finite object. The scattered waves form a diffraction pattern on the Ewald sphere, which can be expressed in the spherical polar coordinate system as (supplementary discussion)

$$|F(\theta, \varphi)| = \left| \int_V \rho(\vec{r}) e^{-\frac{2\pi i}{\lambda} [x \sin \theta \cos \varphi + y \sin \theta \sin \varphi + z(\cos \theta - 1)]} d^3 \vec{r} \right| \quad (1)$$

where $|F(\theta, \varphi)|$ is proportional to the magnitude of the scattered waves, θ and φ the spherical polar coordinates, $\rho(\vec{r})$ the 3D structure of the object with $\vec{r} = (x, y, z)$, and V the spatial extent of the object. When the 2D spherical diffraction pattern is sampled at a scale sufficiently finer than the Nyquist interval such that the oversampled degree (O_d) is larger than 1, the oversampled diffraction pattern in principle determines the 3D structure of the object (supplementary discussion), which can be retrieved by iterative algorithms. Here the oversampled degree is defined as the ratio of the number of measured intensity points from Eq. (1) to the number of unknown variables of the 3D object array²⁸. The 3D spatial resolution of ankylography is determined by (supplementary Fig. S1)

$$d_x = d_y = \frac{\lambda}{\sin(2\theta_{\max})} \quad d_z = \frac{\lambda}{2 \sin^2 \theta_{\max}} \quad (2)$$

where d_x , d_y and d_z represent the resolution along the X, Y and Z-axes, respectively. The Z-axis is along the beam propagation direction and $2\theta_{\max}$ is the diffraction angle shown in Fig. 1.

To confirm our theoretical analysis, we conducted numerical simulations on 3D structure determination of sodium silicate glasses (25Na₂O-75SiO₂). Sodium silicate glasses are archetypal for a wide variety of multicomponent silicate glasses that find

applications from glassware and window panes, to optical fibers, photonic devices and bioactive glasses. Unlike crystalline materials, glasses lack long-range periodicity, which makes experimental determination of the glass structure difficult by traditional diffraction methods. Thus, the inherent complexity of glass structures combined with the lack of experimental methods to probe them (especially for medium range structures) make understanding and visualizing the atomic and nanostructure of glasses a great challenge to the scientific community. By combining classical molecular dynamics (MD) simulations with subsequent geometry optimization using *ab initio* density functional theory calculations, we obtained a 3D sodium silicate glass structure of 204 atoms, with a size of $14 \times 14 \times 14$ Å (supplementary methods). A beam of coherent X-rays with a wavelength of 2 Å was incident on the nanostructure. The total coherent flux illuminating the glass structure was about 10^{13} photons. An oversampled 2D diffraction pattern was calculated on the Ewald sphere, with $2\theta_{\max} = 90^\circ$. Poisson noise was added to the spherical diffraction pattern, shown in Fig. 1a.

To reconstruct the 3D glass structure, we embedded the 2D spherical diffraction pattern into a 3D array of 64^3 voxels, corresponding to $O_d = 2.7$. Since the electron density of the glass structure is real, we also embedded the centro-symmetrical diffraction pattern into the same array. All the other data points in the 3D array were set as unknowns. The 3D image reconstruction was carried out using an iterative phase retrieval algorithm (Methods). Figure 1b shows the 3D atomic positions of the reconstructed sodium silicate glass structure with a resolution of 2 Å in all three dimensions. In Fig. 1b, the red, purple and yellow spheres represent the positions of O, Na and Si atoms, respectively. Compared to the MD simulated structure, the 3D atomic positions of the sodium silicate glass structure are resolved. Figure 2 shows two 2-Å-

thick slices of the MD simulations (Figs. 2a and c) and the reconstructed structures (Figs. 2b and d) along the XY and XZ planes, respectively. The electron density distribution of the reconstructed structure is in good agreement with that of the MD simulation. The slight difference of the electron density between the two structures is likely due to the Poisson noise added to the diffraction pattern.

To experimentally verify ankylography, we used an EUV laser with a wavelength of 47 nm and $\lambda/\Delta\lambda \approx 10^4$ (ref. 24). A test pattern was fabricated by etching through a substrate consisting of a silicon nitride membrane of ~200 nm thick. Except for the patterned area, the substrate is completely opaque to the 47 nm EUV light. To increase the Z-axis depth of the test sample, we slanted the sample relative to the incident beam (Fig. 3b). At a distance of 14.5 mm from the sample mounted a CCD camera (Andor) with 2048×2048 pixels and a pixel size of 13.5×13.5 μm . A 2D diffraction pattern was measured by the detector with intensities extending to the edges of the CCD camera. To enhance the signal to noise ratio, we integrated the diffraction intensities by binning 3×3 pixels into 1 pixel and then interpolated the planar diffraction pattern onto the Ewald sphere (supplementary discussion, Fig. 3a). The spherical diffraction pattern was embedded into a 3D array of 420×420×240 voxels with $O_d = 2.6$.

The phase retrieval was carried out using similar methods to those used for the sodium silicate glass structure (Methods). Figs. 3b and c show iso-surface renderings of the 3D reconstruction in the XY plane (front view) and the XZ plane (side view), respectively, in which the front view is in good agreement with the SEM image (Fig. 3e). The spatial resolution of the reconstructed image was estimated to be 80 nm along the X and Y-axes and 140 nm along the Z-axis. Based on the 3D reconstruction, we accurately measured the tilt angle of the sample relative to the beam to be 4.5° (Fig. 3b).

Fig. 3d shows a lineout across the 3D reconstructed image. The thickness of the sample was determined to be 210 nm, which is consistent with the known value of ~200 nm. Moreover, we identified two structure defects in the SEM image of the test sample (arrows in Fig. 3e). The structure defects are clearly resolved in the reconstructed image (arrows in Fig. 3b), which further confirms the robustness of our 3D reconstruction method.

In conclusion, we have discovered that the 3D structure information of a finite object is encoded into a 2D diffraction pattern on the Ewald sphere. When the diffraction pattern is sufficiently oversampled, the 3D structure can be directly retrieved from the 2D spherical diffraction pattern alone. Both our numerical simulations and experimental results have verified the feasibility of this novel 3D imaging technique. Compared to conventional 3D coherent diffraction microscopy^{7,10-13,16,19}, ankylography requires a comparable amount of incident flux for achieving a desired resolution, but redistributes all the intensity points more finely on the Ewald sphere, which eliminates the necessity of sample tilting. By properly choosing the wavelength of the monochromatic incident beam, ankylography can in principle be implemented using synchrotron radiation, high harmonic and short wavelength laser sources, optical lasers, electrons, and X-ray free electron lasers. Thus we expect the applications of ankylography to be broad across several disciplines. In biology, as optical diffraction microscopy has already been applied to imaging a biological sample²², ankylography may open a door for 4D optical imaging of biological specimens since sample tilting, scanning or sectioning can be avoided. With X-FELs, ankylography will enable 3D structure determination of a biological specimen from a single pulse before the specimen is destroyed^{25,29}. In materials science, ankylography can in principle be

applied to investigating time-resolved 3D structure of disordered materials using X-FELs.

Methods

The 3D phase retrieval algorithm in ankylography. 3D image reconstructions for both the simulated glass structure and the experimental data were carried out using an iterative phase retrieval algorithm. The algorithm begins with a random phase set as an initial input and iterates back and forth between Fourier and real space. Physical constraints were applied in each space. In Fourier space, the magnitudes of the Fourier transform on the Ewald sphere were set to the measured values. The data points not on the Ewald sphere (*i.e.* not measured) were initially set as unknowns and updated with each iteration of the reconstruction. In real space, three constraints were enforced: the electron density must be positive, real-valued and bounded within the spatial extent of the sample (*i.e.* a support). Data points of the image estimate that didn't satisfy these constraints were modified by the operations described in the hybrid input-output algorithm³⁰. After 13,000 iterations, the algorithm was further perturbed once every ten iterations over a period of 10,000 iterations by using a smoothness function which was applied to the image estimate outside the support,

$$\rho_j^{new}(\vec{r}) = \rho_j(\vec{r}) \otimes \Pi(\vec{r}) \quad \text{for } \vec{r} \notin S \quad (3)$$

where $\rho_j(\vec{r})$ and $\rho_j^{new}(\vec{r})$ represent the j^{th} image estimate and the smoothed image, respectively, \otimes represents the convolution operation, $\Pi(\vec{r})$ is the unit step function over a $4 \times 4 \times 4$ voxel volume and S is the support. Eq. (3) reduces the fluctuations outside the support which is a known physical constraint. An error metric, defined as the difference between the computed data points on the Ewald sphere and the measured ones, was used to monitor the convergence of the algorithm. Compared to the phase retrieval in coherent diffraction microscopy⁵⁻²⁷, the ankylographic reconstruction generally demands more computational resources, which is natural since the traditional phase retrieval problem is to recover $\rho(\vec{r})$ from $|F(\vec{k})|$. Yet in ankylography, the measured intensity only spans some small but dense subspace of the reciprocal domain. Our simulation studies have shown that the convergence of the iterative algorithm is related to the size of the sample under investigation; additional physical constraints such as atomicity and phase extension may be used to expedite the convergence. Finally, by using two or

more 2D spherical diffraction patterns (*i.e.* two or more sample tilts), we found that the convergence of the algorithm can be significantly sped up.

References

1. Giacobazzo, C. *et al.* *Fundamentals of Crystallography*. Oxford University Press, USA, 2nd edition (2002).
2. Kak, A.C. & Slaney, M. *Principles of Computerized Tomographic Imaging*. (SIAM, Philadelphia, 2001).
3. *Handbook of Biological Confocal Microscopy*. Edited by J. B. Pawley, 3rd Ed. (Springer, 2006).
4. Sayre, D. in *Imaging Processes and Coherence in Physics* vol. **112**, (eds Schlenker, M. *et al.*) 229-235 (Lecture Notes in Physics, Springer, 1980).
5. Miao, J., Charalambous P., Kirz, J. & Sayre, D. Extending the methodology of X-ray crystallography to allow imaging of micrometre-sized non-crystalline specimens. *Nature* **400**, 342 (1999).
6. Robinson, I. K., Vartanyants, I. A. ,Williams, G. J., Pfeifer, M. A. & Pitney, J. A. Reconstruction of the Shapes of Gold Nanocrystals Using Coherent X-Ray Diffraction. *Phys. Rev. Lett.* **87**, 195505 (2001).
7. Miao, J. *et al.* High Resolution 3D X-Ray Diffraction Microscopy. *Phys. Rev. Lett.* **89**, 088303 (2002).
8. Miao, J., Hodgson, K. O., Ishikawa, T., Larabell, C. A., LeGros, M. A. & Nishino, Y. Imaging whole Escherichia coli bacteria by using single-particle x-ray diffraction. *Proc. Natl. Acad. Sci. USA* **100**, 110 (2003).
9. Nugent, K. A., Peele, A. G., Chapman, H. N. & Mancuso, A. P. Unique Phase Recovery for Nonperiodic Objects. *Phys. Rev. Lett.* **91**, 203902 (2003).
10. Shapiro, D. *et al.* Biological imaging by soft x-ray diffraction microscopy, *Proc.*

- Natl. Acad. Sci. USA* **102**, 15343-15346 (2005).
11. Pfeifer, M. A., Williams, G. J., Vartanyants, I. A., Harder, R. & Robinson, I. K. Three-dimensional mapping of a deformation field inside a nanocrystal. *Nature* **442**, 63 (2006).
 12. Miao, J. *et al.* Three-dimensional GaN-Ga₂O₃ core shell structure revealed by x-ray diffraction microscopy. *Phys. Rev. Lett.* **97**, 215503 (2006).
 13. Chapman, H. N. *et al.* High resolution *ab initio* three-dimensional x-ray diffraction microscopy. *J. Opt. Soc. Am. A.* **23**, 1179-200 (2006).
 14. Williams, G. J. *et al.* Fresnel Coherent Diffractive Imaging. *Phys. Rev. Lett.* **97**, 025506 (2006).
 15. Abbey, B. *et al.* Keyhole coherent diffractive imaging. *Nature Phys.* **4**, 394 (2008).
 16. Jiang H. *et al.* Nanoscale Imaging of Mineral Crystals inside Biological Composite Materials Using X-Ray Diffraction Microscopy. *Phys. Rev. Lett.* **100**, 038103 (2008).
 17. Thibault, P. *et al.* High-Resolution Scanning X-ray Diffraction Microscopy. *Science* **321**, 379-382 (2008).
 18. Song, C. *et al.* Quantitative Imaging of Single, Unstained Viruses with Coherent X-rays. *Phys. Rev. Lett.* **101**, 158101 (2008).
 19. Nishino, Y., Takahashi Y., Imamoto N., Ishikawa, T. & Maeshima, K. Three-Dimensional Visualization of a Human Chromosome Using Coherent X-Ray Diffraction. *Phys. Rev. Lett.* **102**, 018101 (2009).
 20. Zuo, J. M., Vartanyants, I., Gao M., Zhang R. & Nagahara L. A. Atomic Resolution Imaging of a Carbon Nanotube from Diffraction Intensities. *Science*

- 300**, 1419-1421 (2003).
21. Spence J. C. H., Weierstall U. & Howells M. R. Phase recovery and lensless imaging by iterative methods in optical, X-ray and electron diffraction. *Philos. Trans. R. Soc. London, Ser. A* **360**, 875–895 (2002).
 22. Thibault P. & Rankenburg I. Optical Diffraction Microscopy in a Teaching Laboratory. *Am. J. Phys.*, **75** (9) 827-832 (2007).
 23. Sandberg, R. L. *et al.* Lensless Diffractive Imaging Using Tabletop Coherent High-Harmonic Soft-X-Ray Beams. *Phys. Rev. Lett.* **99**, 098103 (2007).
 24. Sandberg, R. L. *et al.* High Numerical Aperture Tabletop Soft X-ray Diffraction Microscopy with 70 nm Resolution. *Proc. Natl. Acad. Sci. USA* **105**, 24-27 (2008).
 25. Chapman, H. N. *et al.* Femtosecond diffractive imaging with a soft-X-ray free-electron laser. *Nature Phys.* **2**, 839-843 (2006).
 26. Barty, A. *et al.* Ultrafast single-shot diffraction imaging of nanoscale dynamics *Nature Photon.* **2**, 415-419 (2008).
 27. Mancuso, A. P. *et al.* Coherent-Pulse 2D Crystallography Using a Free-Electron Laser X-Ray Source. *Phys. Rev. Lett.* **102**, 035502 (2009).
 28. Miao J., Sayre D. & Chapman H. N. Phase retrieval from the magnitude of the Fourier transforms of non-periodic objects. *J. Opt. Soc. Am. A* **15**:1662-1669 (1998).
 29. Neutze, R., Wouts, R., Spoel D., Weckert, E. & Hajdu, J. Potential for biomolecular imaging with femtosecond X-ray pulses. *Nature* **406**, 752-757 (2000).
 30. Fienup, J. R. Reconstruction of an object from the modulus of its Fourier

transform. *Opt. Lett.* **3**:27-29 (1978).

Acknowledgements We thank C. Song for performing data analysis, Y. Mao for implementing an interpolation code, A. E. Sakdinawat for fabricating a test sample, P. Wachulak, M. Marconi, C. Menoni and J. J. Rocca for help with data acquisition, T. Singh for parallelization of our phase retrieval codes, and B. P. Fahimian for stimulating discussions. This work was supported by the U.S. Department of Energy, Office of Basic Energy Sciences and the U.S. National Science Foundation, Division of Materials Research and Engineering Research Center.

Author information The authors declare no competing financial interests. Correspondence and requests for materials should be addressed to J. M. (miao@physics.ucla.edu).

Figure legends

Figure 1. Schematic layout of the experimental set-up for ankylography. A coherent beam with wavelength λ illuminates a finite object and the scattered waves form a diffraction pattern on the Ewald sphere **(a)**, where $2\theta_{\max}$ represents the diffraction angle. When the diffraction pattern is sampled at a scale sufficiently finer than the Nyquist interval, the 3D structure of the object is encoded into the 2D spherical pattern and can be retrieved by the iterative phase retrieval algorithm **(b)**.

Figure 2. 3D image reconstruction of a sodium silicate glass structure at 2 Å resolution from a 2D spherical diffraction pattern alone. Electron density distribution of a 2-Å-thick slice of the MD simulation **(a)** and the reconstructed structure **(b)** along the XY plane where the red, purple and yellow spheres represent the positions of O, Na and Si atoms, respectively. Electron density distribution of a 2-Å-thick slice of the MD simulation **(c)** and the reconstructed structure **(d)** along the XZ plane.

Figure 3. Experimental demonstration of ankylography by using a soft X-ray laser with a wavelength of 47 nm. **a**, Oversampled 2D diffraction pattern on the Ewald sphere. Iso-surface renderings of the 3D reconstructed image in the XY plane (**b**) and XZ plane (**c**), respectively, where the incident beam is along the Z-axis. **d**, Lineout indicating the thickness of the test sample to be 210 nm. **e**, SEM image of the sample (scale bar = 1 μm). Insets show two structure defects (labelled with arrows) in the test sample which are confirmed by the 3D reconstruction (arrows in **b**).

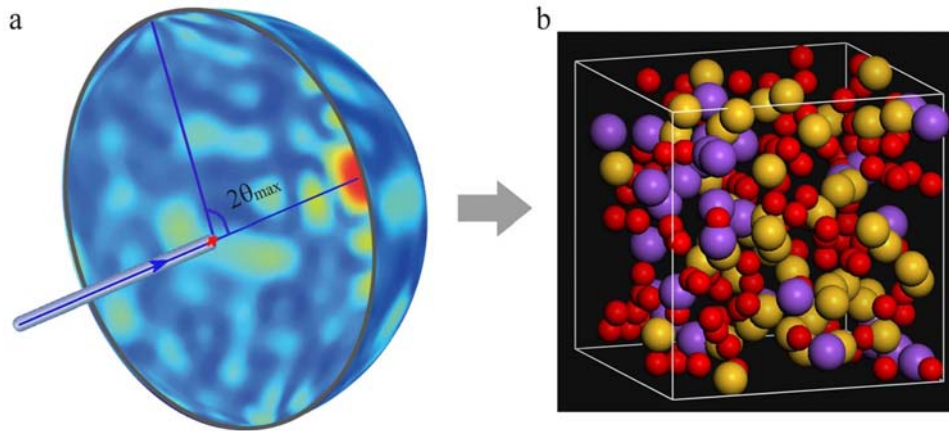


FIG. 1

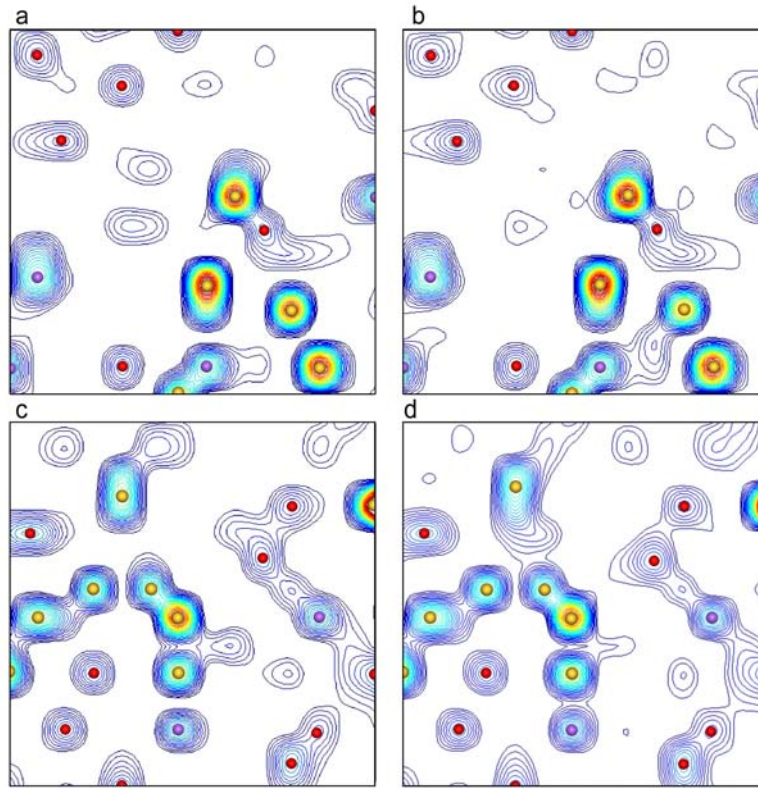


FIG. 2

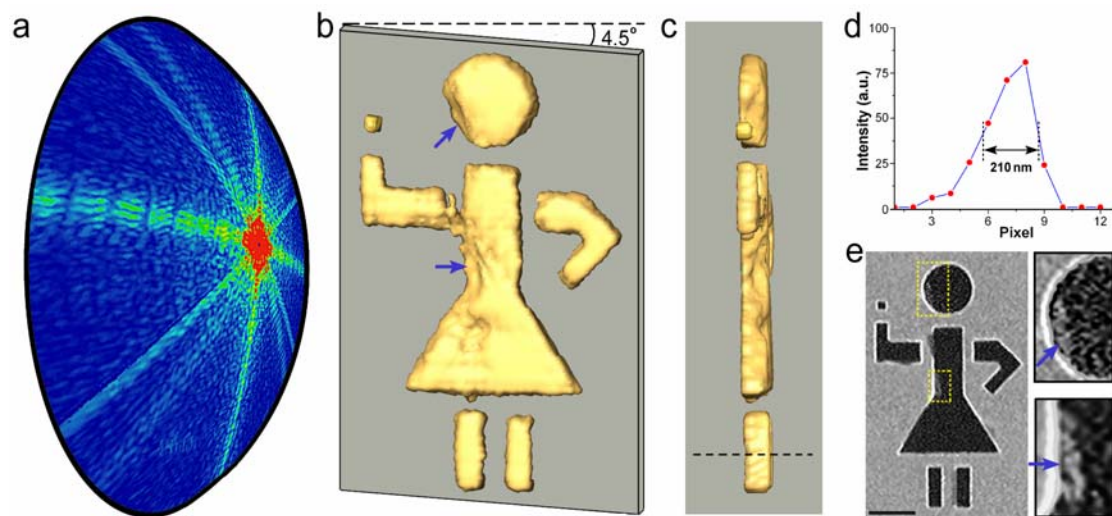


FIG. 3

SUPPLEMENTARY INFORMATION

Kevin S. Raines¹, Sara Salha¹, Huaidong Jiang¹, Richard L. Sandberg², Henry C.

Kapteyn², Margaret M. Murnane², Jincheng Du³ and Jianwei Miao¹

¹Department of Physics and Astronomy and California NanoSystems Institute, University of California, Los Angeles, CA 90095, USA. ²Department of Physics and JILA, University of Colorado and NIST, Boulder, CO 80309, USA. ³Department of Materials Science & Engineering, University of North Texas, Denton, TX 76203, USA

This file contains Supplementary Methods, Supplementary Discussion with Supplementary Figs. 1-4 and legends, and Supplementary References.

Supplementary Methods

The 25Na₂O-75SiO₂ glass structure was obtained by combining classical molecular dynamics (MD) simulations and subsequent geometry optimization using *ab initio* Density Functional Theory (DFT) calculations. Final electron density for both core and valence electrons was calculated using the DFT based on the optimized geometry. The simulation cell contains 204 atoms in a cubic box of 14×14×14 Å³ dimension to give the glass density of ~ 2.43 g/cc. The simulated melt and quench procedure was used to generate the glass structure by MD simulations with partial charge potentials as described elsewhere¹. Starting from randomly generated initial atom positions, the system was first melted at 6000 K and then equilibrated at 4000 K, each with 100 ps NVT run and subsequent 100 NVE run. From 4000 K, the melt was then cooled down to 300 K by

gradually decreasing the temperature at a cooling rate of 10 K/ps. At 300 K, the glass was equilibrated for 200 ps NVT runs and 200 ps NVE runs. Glass structure from MD simulation was further optimized using plane wave basis set, gradient corrected DFT calculations carried out using the Vienna *ab initio* Simulation Package (VASP) at highly parallel super computers. Projected Augmented Wave (PAW) pseudopotential and the PBE exchange and correlation function was used in the DFT calculations. Gamma point only K point sampling was used due to large simulation cell in our calculations. A plane wave kinetic energy cutoff of 400 eV was used. The convergence criterion for electronic SCF was $1e^{-4}$ eV and geometry optimization was stopped when the forces acting on atoms were smaller than 0.01 eV/Å. Based on the optimized structure, total electron density (both core and valence electrons) were generated on a grid for subsequent image reconstruction.

Supplementary Discussion

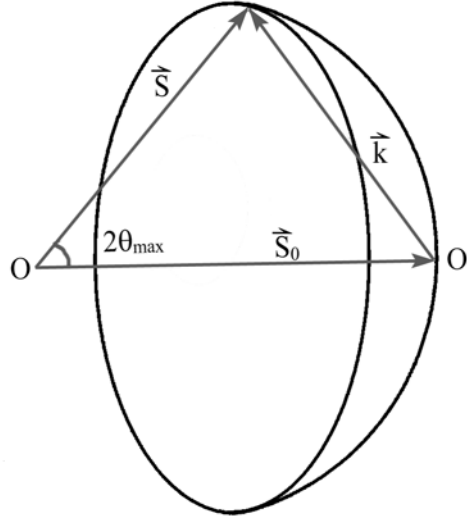
1. Representation of a 2D diffraction pattern on the Ewald sphere

Based on the Born approximation, the 3D diffraction intensities of a finite object can be represented as

$$\left| F(\vec{k}) \right| = \left| \int_V \rho(\vec{r}) e^{-2\pi i \vec{k} \cdot \vec{r}} d^3\vec{r} \right| \quad (S1)$$

where $\left| F(\vec{k}) \right|$ is proportional to the square root of the diffraction intensities,

$\vec{k} = (k_x, k_y, k_z)$ is the reciprocal-space vector, $\rho(\vec{r})$ is the 3D structure of the object with



Supplementary Fig. S1 Geometrical construction of the wave vectors and the Ewald sphere. \vec{S}_0 and \vec{S} are the incident and scattered wave vectors with $|\vec{S}_0| = |\vec{S}| = \frac{1}{\lambda}$, and λ is the wavelength of the incident beam. O is the origin of the Ewald sphere and O' is the origin of \vec{k} .

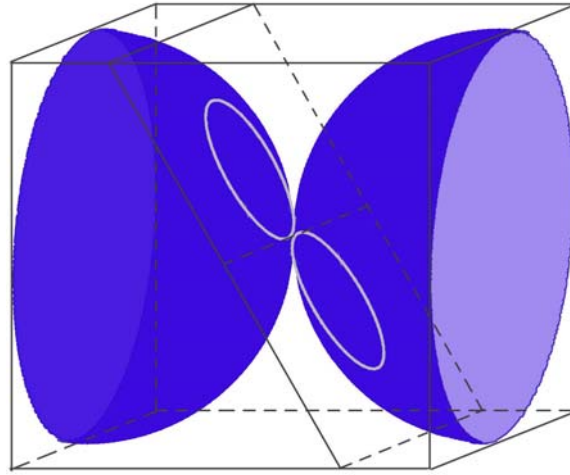
$\vec{r} = (x, y, z)$, and V is the spatial extent of the object. To calculate the diffraction intensities on the Ewald sphere, we constructed a geometrical representation of the Ewald sphere, shown in Fig. S1. By expressing \vec{k} in the spherical polar coordinates, we have

$$\begin{aligned} k_x = S_x &= \frac{1}{\lambda} \sin \theta \cos \phi \\ k_y = S_y &= \frac{1}{\lambda} \sin \theta \sin \phi \\ k_z = S_z - S_0 &= \frac{1}{\lambda} (\cos \theta - 1) \end{aligned} \quad (\text{S2})$$

where \vec{S}_0 and \vec{S} are the incident and scattered wave vectors with $\vec{S} = (S_x, S_y, S_z)$, θ and ϕ are the spherical polar coordinates, and λ is the wavelength of the incident beam. By substituting Eq. (S2) into Eq. (S1), we obtained Eq. (1) in the manuscript.

2. An oversampled 2D diffraction pattern on the Ewald sphere determines the 3D structure of a finite object

Here we present a physical explanation on why an oversampled 2D diffraction pattern on the Ewald sphere determines the 3D structure of a finite object. For the purpose of clarity, we focus on a real object, but our arguments remain valid for a complex object. Figure S2 shows an oversampled diffraction pattern on the Ewald sphere with the diffraction angle $2\theta_{max} = 90^\circ$. The presence of the diffraction patterns on two hemispheres comes from the centro-symmetry of the intensities. The question of the uniqueness can be addressed from the relationship of the Ewald sphere to a central projection. According to the Fourier slice theorem, the Fourier transform of the central projection of a 3D object is equal to a Fourier slice through the origin of the 3D Fourier transform of the object at a given angle². Figure S2 shows a central Fourier slice intersecting with the diffraction pattern on



Supplementary Fig. S2 Intersection between a Fourier slice and the Ewald sphere at a give angle, forming a circle, an arc or a point. The two hemispheres are due to the centro-symmetry of the diffraction intensities and the X-axis is the rotation axis.

the Ewald sphere and forming a circle. When the 3D object is rotated around the X-axis, the intersection between the Ewald sphere and the corresponding central Fourier slice will either form a circle, an arc or a point, which can be expressed as

$$e_\alpha = D_E \cap P_\alpha \quad (\text{S3})$$

where e_α represents the intersection at a given rotation angle α along the X-axis, \cap is the intersect operation, D_E the diffraction pattern on the Ewald sphere and P_α a central Fourier slice at angle α . When the diffraction pattern is sufficiently oversampled with the oversampling degree $O_d > 1$, D_E is the set consisting of the intersected arcs, circles and point along the all possible rotation angles about the X-axis,

$$D_E = \{0 \leq \alpha < 180^\circ: D_E \cap P_\alpha\} \quad (\text{S4})$$

We have so far restricted the discussion to the case of rotation about the X-axis. However, we note that the oversampled diffraction pattern on the Ewald sphere can be constructed by rotating about either X, Y or Z-axis, where the argument is repeated. We hence have

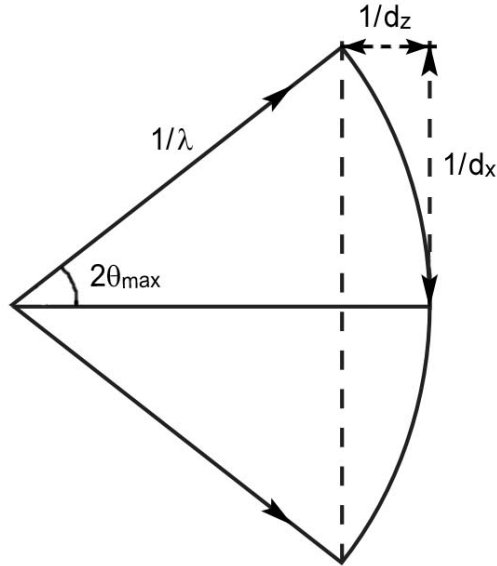
$$D_E = \{0 \leq \alpha, \beta, \gamma < 180^\circ: D_E \cap P_\alpha, D_E \cap P_\beta, D_E \cap P_\gamma\} \quad (\text{S5})$$

where β and γ are the rotation angles about the Y and Z-axis, respectively. Eq. (S5) indicates that the oversampled diffraction pattern on the Ewald sphere is the set consisting of the intersected arcs, circles and point in *all possible* orientations. If two 3D objects share exactly the same oversampled diffraction pattern on the Ewald sphere, they must possess the identical intersected arcs and circles of the central Fourier slices in *all possible* orientations and have to be physically equivalent on the basis of equivalent projections. To further confirm ankylography, we perform numerical simulations in the

manuscript to show that the 3D object is not only unique but also recoverable – a more difficult condition to fulfill.

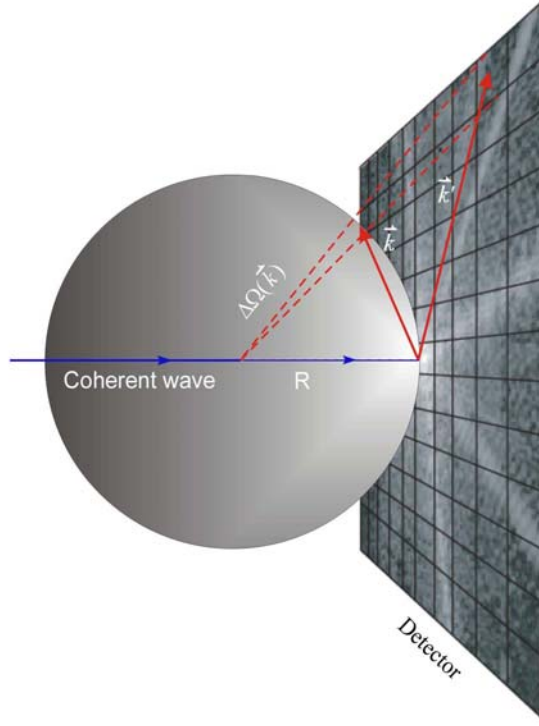
3. 3D spatial resolution in ankylography

Figure S3 shows a cross-section of a 2D diffraction pattern on the Ewald sphere. The spatial resolution along the X, Y and Z-axes is d_x , d_y and d_z , respectively, where $d_x = d_y$ is due to the spherical symmetry. Based on this geometrical construction (Fig. S3) and Bragg's law, we obtained Eq. (2) in the manuscript.



Supplementary Fig. S3 Cross-section of a 2D diffraction pattern on the Ewald sphere illustrating the 3D spatial resolution in ankylography. The resolution along the X and Z-axis are d_x and d_z , respectively, $2\theta_{\max}$ is the diffraction angle and $1/\lambda$ is the radius of the Ewald sphere.

4. Interpolation of a planar diffraction pattern onto the Ewald sphere



Supplementary Fig. S4 Projection of an oversampled 2D diffraction pattern from a planar detector onto the Ewald sphere, where $\vec{k} = (k_x, k_y, k_z)$ is a vector on the Ewald sphere, $\vec{k}' = (k'_x, k'_y)$ a vector on the detector plane and $\Delta\Omega(\vec{k})$ a solid angle subtended by the pixel area.

Since the diffraction pattern was measured by a planar CCD detector, in order to perform 3D phase retrieval, the diffraction intensities have to be normalized³ and then projected onto the Ewald sphere. As Fig. S4 shows, each pixel of the planar detector integrates the diffracted photons within a solid angle, $\Delta\Omega(\vec{k})$, subtended by the pixel area. Since $\Delta\Omega(\vec{k})$ decreases with the increase of the spatial frequency, we normalize the diffraction intensities by

$$I(\vec{k}) = \frac{I_M(\vec{k})}{\Delta\Omega(\vec{k})} \quad (\text{S6})$$

where $I(\vec{k})$ and $I_M(\vec{k})$ are the normalized and measured intensities.

After the normalization, the diffraction intensities have to be projected onto the Ewald sphere. Based on the geometry shown in Fig. S4, we obtain the relationship between the vector on the Ewald sphere (\vec{k}) and the vector on the detector plane (\vec{k}'),

$$\begin{aligned} k_x &= \frac{Rk'_x}{\sqrt{R^2 + k'^2_x + k'^2_y}} \\ k_y &= \frac{Rk'_y}{\sqrt{R^2 + k'^2_x + k'^2_y}} \\ k_z &= R \left(1 - \frac{R}{\sqrt{R^2 + k'^2_x + k'^2_y}} \right) \end{aligned} \quad (S7)$$

where $\vec{k} = (k_x, k_y, k_z)$ is a vector on the Ewald sphere, $\vec{k}' = (k'_x, k'_y)$ is a vector on the 2D planar detector, and R the distance from the sample to the detector. As Fig. S4 shows, k'_x and k'_y are on a regular 2D grid, but k_x , k_y and k_z are on an irregular 3D grid. Since a regular 3D grid in Fourier space is mandatory for the phase retrieval algorithm due to the use of the FFT, we interpolate $I(\vec{k})$ onto a regular 3D Cartesian grid by using a linear interpolation method².

Supplementary References

1. Du, D. & Corrales, L. R. Compositional dependence of the first sharp diffraction peaks in alkali silicate glasses: A molecular dynamics study. *J. Non-Cryst. Solids*, **352**, 3255-3269 (2006).
2. Kak, A.C. & Slaney, M. *Principles of Computerized Tomographic Imaging*. (SIAM, Philadelphia, 2001).
3. Song, C. *et al.* Phase Retrieval from Exactly Oversampled Diffraction Intensity Through Deconvolution. *Phys. Rev. B*. **75**, 012102 (2007).